JACS
JOURNAL OF THE AMERICAN CHEMICAL SOCIETY

Article

pubs.acs.org/JACS

CVD Growth of Carbon Nanostructures from Zirconia: Mechanisms and a Method for Enhancing Yield

Akira Kudo,[†] Stephen A. Steiner, III,[‡] Bernhard C. Bayer,[§] Piran R. Kidambi,[§] Stephan Hofmann,[§] Michael S. Strano,[∥] and Brian L. Wardle*[,‡]

[†]Department of Materials Science and Engineering, Massachusetts Institute of Technology, 77 Massachusetts Avenue, Cambridge, Massachusetts 02139, United States

[‡]Department of Aeronautics and Astronautics, Massachusetts Institute of Technology, 77 Massachusetts Avenue, Cambridge, Massachusetts 02139, United States

[§]Department of Engineering, Electrical Engineering Division, University of Cambridge, 9 JJ Thomson Avenue, Cambridge CB3 0FA, United Kingdom

[∥]Department of Chemical Engineering, Massachusetts Institute of Technology, 77 Massachusetts Avenue, Cambridge, Massachusetts 02139, United States

Supporting Information

ABSTRACT: By excluding metals from synthesis, growth of carbon nanostructures via unreduced oxide nanoparticle catalysts offers wide technological potential. We report new observations of the mechanisms underlying chemical vapor deposition (CVD) growth of fibrous carbon nanostructures from zirconia nanoparticles. Transmission electron microscope (TEM) observation reveals distinct differences in morphological features of carbon nanotubes and nanofibers (CNTs and CNFs) grown from zirconia nanoparticle catalysts versus typical oxide-supported metal nanoparticle catalysts. Nanofibers borne from zirconia lack an observable graphitic cage consistently found with nanotube-bearing metal nanoparticle catalysts. We observe two distinct growth modalities for zirconia: (1) turbostratic CNTs 2−3 times smaller in diameter than the nanoparticle localized at a nanoparticle corner, and (2) nonhollow CNFs with approximately the same diameter as the nanoparticle. Unlike metal nanoparticle catalysts, zirconia-based growth should proceed via surface-bound kinetics, and we propose a growth model where initiation occurs at nanoparticle corners. Utilizing these mechanistic insights, we further demonstrate that preannealing of zirconia nanoparticles with a solid-state amorphous carbon substrate enhances growth yield.

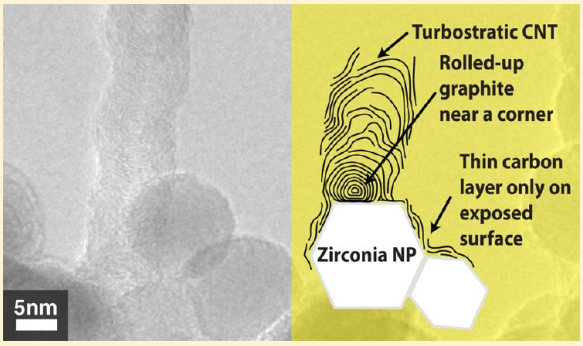

INTRODUCTION

From high-strength fibers[1,2] to CMOS-compatible processing[3,4] and cancer diagnostics,[5] numerous potentially high-impact applications made possible by nanostructured carbon materials are complicated by the presence of residual metals. Accordingly, many researchers have set out to create processes that enable growth of carbon nanostructurs such as carbon nanotubes (CNTs), carbon nanofibers (CNFs), and graphene without the use of metals.[6−8] For nanotubes and nanofibers, promising candidates to date have included metal oxides (e.g., zirconia,[9] alumina,[10] titania,[11] tantala,[12] and silica[13]), as well as a number of other unconventional catalyst materials such as metalloid nanoparticles[14] and nanodiamond.[15] These metal oxides are presumed not to reduce carbothermically during CVD growth, as opposed to, e.g., iron oxide, which is known to reduce during CVD. From a growth standpoint, unreduced oxides offer several advantages over metals including chemical inertness on many substrates, high-temperature stability, resistance to carburization, and shape stability, opening new avenues for device integration, chirality control, and catalyst lifetime extension. Hierarchical structural composites reinforced with aligned CNTs are one example where growth using nonmetallic catalysts would be advantageous, as direct growth of CNTs on carbon fibers with metal catalysts has been shown to significantly damage the strength properties of the underlying fiber.[16] Nanotube-based electrodes for energy storage devices are another example[17] where residual metal nanoparticle catalysts can cause degradation of performance, as metal catalysts can interact with the electrolyte and positive charge carriers resulting in formation of undesired compounds inside the cell.

Perhaps the most significant issue stifling routine adoption of oxide-mediated CVD growth of carbon nanostructures is that, to date, processes employing such catalysts typically result in substantially lower yields of carbon nanostructures than conventional metal nanoparticle catalysts (e.g., Fe, Co/Mo, Ni,

Received: September 24, 2014
Published: December 9, 2014

   dx.doi.org/10.1021/ja509872y | J. Am. Chem. Soc. 2014, 136, 17808−17817

etc.). Despite attempts to improve yield via parametric optimization of process conditions,[18] a reliable process for reproducible growth of CNTs and CNFs that yields comparable areal density and nanostructure lengths to metal catalysts remains elusive. While clearly different than growth from metals, fundamental aspects of the mechanistic models for metal oxide catalysts are still missing, as discussed in a recent review.[19] In general, growth of CNTs and CNFs from metal nanoparticle catalysts involves (1) vapor-phase thermal recombination of carbon-containing feedstocks,[20] (2) further catalytic decomposition at the metal surface, and (3) concomitant precipitation and assembly of carbon into the carbon nanostructure.[21] Many groups have previously postulated that CNT growth proceeds via a vapor−liquid−solid (VLS) mechanism;[22,23] however, it is now known that growth via VLS is not universal. For example, in situ TEM imaging[24,21] and crystallographic analysis[25] have shown that growth with metal catalysts such as Fe and Ni involves the reduced metal and may or may not involve transition of the catalyst to a liquid or liquid-like phase. CVD growth of CNTs employing substances such as Re nanoparticles further indicates that CNT growth does not require a liquid phase catalyst, since the solubility of carbon in bulk Re is very low, and Re has a high bulk melting temperature (∼3185 °C) well beyond observed CNT growth temperatures.[26] The mechanism of growth employing unreduced oxides likely proceeds via a different route than growth employing metals, as the propensity of such oxides to catalyze reactions with hydrocarbons differs from metals, the melting temperatures of such oxides are much higher than typical CVD growth temperatures, and the diffusivity and solubility of carbon in such oxides is lower than in metals like iron.[27] For these reasons, the mechanism of CVD growth employing oxide nanoparticle catalysts has been suggested to proceed via a surface-bound process,[28] although this prediction has not been previously demonstrated experimentally.

One challenge in understanding growth from oxide catalysts is deconvolving the potential influence of trace metal contaminants synergistically interacting with oxide nanoparticles from growth resulting from pure oxide nanoparticles. For example, oxide supports are frequently used in conjunction with metal catalysts to improve growth yield from metal catalysts, e.g., alumina is used as a support for iron nanoparticle catalysts in the growth of high-yield aligned-CNT forests.[29,30] In this example, alumina acts as a solid-state electrophile (acid) that activates the iron for CNT growth thereby improving growth yield.[31] Given the general low efficiency of standalone oxide nanoparticle catalysts when compared to metal nanoparticle catalysts subjected to similar conditions, one might question whether or not oxide nanoparticles are active toward carbon nanostructure growth at all or if the growth that is observed with these substances is actually a result of transient metal contaminants commonly present in such experiments. However, in situ XPS and ex situ TEM studies of zirconia nanoparticle catalysts,[9] in addition to quasi in situ lattice-fringe-resolved HRTEM imaging of silica nanoparticle catalysts,[32] provide clear support that some oxide nanoparticles do indeed serve as growth catalysts. These works show that the nanoparticle catalysts are not reduced to a nonoxide state during CVD, which has been frequently questioned especially for silica and oxides with similar reduction potential in the metal−oxygen Ellingham diagram.[19]

In this work, differences in the morphologies of carbon nanostructures grown from a metal oxide catalyst (zirconia) and conventional oxide-supported metal catalysts (zirconia-supported Fe and Cr) are investigated using HRTEM and localized EDX analysis. We synthesized carbon nanostructures (CNTs and CNFs of varying morphologies) directly on TEM grids on which oxide nanoparticles were spatially separated from oxide-supported metal nanoparticle catalysts on the same grid. By spatially resolving these two types of catalyst systems on the same grid, we were able to grow nanostructures from both systems simultaneously while ensuring identical growth conditions for both catalysts, thereby eliminating potential differences that may arise due to process parameter variations. We find that zirconia-grown and metal-grown carbon nanostructures are clearly distinguishable by morphological features present in the carbon nanostructure itself as well as environment surrounding the catalyst particle, providing experimental support that growth with zirconia proceeds via a surface-bound mechanism. Growth was performed on both lacy-carbon-coated Cu TEM grids and metal-free SiN grids and comparable results were obtained with both types. This verified that the observed growth does not result from interactions with Cu and validated the localized analysis approach as a rigorous means for characterizing catalysts and mechanisms. On the basis of these observations, we propose a growth model that interrelates zirconia nanoparticle, size, shape, and observed intermediary carbon nanostructure features, and use this information to demonstrate a practical method for enhancing the yield of CNTs/CNFs resulting from CVD growth employing zirconia nanoparticles.

EXPERIMENTAL SECTION

Synthesis and Deposition of Zirconia Nanoparticle Catalysts onto TEM Grids. Zirconia nanoparticles were prepared via two different synthetic approaches and deposited onto lacy-carbon-coated TEM grids (Pacific Grid Tech, product number Cu-400LC. 3.05 mm OD copper grid with 30 nm thick lacy carbon film. The lacy carbon film is amorphous and has random holes with mean diameter of 42 μm). In the first approach, saturated dispersions of zirconium(IV) oxychloride octahydrate (Sigma-Aldirch, product number 31670 >99.5%) in isopropyl alcohol (IPA, VWR CAS No 67−63−0, >99.5%) was prepared, and its diluted supernatant is (1 g of the supernatant in 11.45 g of IPA) dropcast onto the TEM grid as previously described[9] to create polydisperse zirconia nanoparticles onto the TEM grid. In the second approach, solutions of monodispersed 4 nm-diameter zirconia nanoparticles synthesized via high-temperature anhydrous sol−gel synthesis according to the method of Joo et al. were used.[33] Solutions were prepared by dispersing 10 mg of nanoparticles in 15.72 g (20 mL) of IPA followed by sonication for 5 min. Dispersed solutions were then dropcast onto the TEM grid. In order to evaluate whether metal adatoms, possibly present from the TEM grid, may affect growth from the spatially separated zirconia nanoparticles on lacy carbon, the same growth process is used on silicon nitride TEM grids (SiN grid, Tedpella, product number 21569−10). Both pristine SiN grids and pyrolytic carbon-coated SiN grids are tested.

Deposition of Metal Nanoparticle Catalysts onto TEM Grids. We controllably introduce metal nanoparticles (of Fe and Cr) onto a part of the TEM grid by contacting the grid with stainless steel tweezers. We have found that contacting substrates with metallic instruments such as stainless steel tweezers deposits catalytically active metal nanoparticles locally at the site of contact. For this reason, in previous studies we have rigorously avoided the use of metallic tools (e.g., by only using plastic tweezers, insertion rods, and storage containers, etc.) to prevent unintended introduction of metals onto catalyst substrates. Here in contrast, the use of metal instruments enabled spatially resolved observation of the growth behavior of both zirconia-supported metallic nanoparticles and isolated pure, unreduced zirconia nanoparticles on different parts of the grid pari passu, i.e., under the same growth conditions, by ex-situ TEM.

Direct CVD Growth of CNTs/CNFs on TEM Grids. CVD and annealing processes were performed in fused quartz process tubes (25 mm OD × 22 mm ID × 76.2 cm length) placed inside a Lindberg/Blue

dx.doi.org/10.1021/ja509872y | J. Am. Chem. Soc. 2014, 136, 17808−17817

M MiniMite 1 inch diameter electric clamshell tube furnace. Process tubes were baked in air at 800 °C for 1 h prior to both CVD and annealing. Argon, hydrogen, and ethylene (Airgas, UHP grade, 99.999%) were used for CVD. Sample grids were first placed on a piece of silicon wafer with silica layer on top and inserted into the process tube about 4 cm passed the zone center toward the exhaust end of the tube. Prior to CVD, samples were thermally treated at 800 °C under a flow of 200 sccm of argon for 60 min and then cooled down to room temperature. CVD processing was then performed as follows. First, the process tube was flushed with 750 sccm of argon at room temperature for 2 min to remove residual air from the tube. Next, a flow of 400 sccm of hydrogen and 100 sccm of argon was introduced and the temperature was ramped to 750 °C. Once at temperature, a flow of 100 sccm of ethylene was added. After 15 min, the hydrogen and ethylene were turned off and the system was cooled to room temperature. CNTs and CNFs synthesized on lacy-carbon-coated Cu TEM grids were then characterized by HRTEM and point-localized EDX (JEOL 2010F). For CNTs and CNFs synthesized on SiN TEM grids we used Cs-corrected HRTEM and EDX (Zeiss Libra 200−80).

FFT Pattern Analysis. FFT patterns of HRTEM images are generated by Gatan Digital Micrograph. Analyzing angles between reflections and lattice distances measured by ImageJ that correspond to each Miller index, we determine if the nanoparticles attached to grown CNTs/CNFs are zirconia and if so the phase of the zirconia nanoparticle. A short script is coded in C to calculate the angles between reflections based on lattice parameters obtained from the literature (monoclinic zirconia,[34] tetragonal zirconia,[35] cubic zirconia,[36] zirconium carbide,[37] Zr,[38] α-Fe,[39] Cr,[40] Cu,[41] copper(I) oxide,[42] copper(II) oxide[43]), and the calculated angles are compared to the angles in FFT patterns. Cu and its oxides are fully investigated in order to distinguish zirconia nanoparticles from Cu and/or copper oxide nanoparticles.

Preparation of Carbon Xerogel- and Aerogel-Supported Zirconia. RF gel precursors were prepared according to the method of Mulik et al.[44] and the method of Pekala et al.,[45] which give comparable results. Briefly, according to the method of Mulik et al., 0.337 g of resorcinol (Sigma-Aldrich, product number W358908, >98%) and 0.447 mL of formaldehyde (Sigma-Aldrich, product number 252549, 37 wt % in water, contains 10−15% of methanol as stabilizer) were added to 11.5 mL of acetonitrile (Sigma-Aldrich, product number 271004, 99.8%) to which a solution of 0.03 mL of concentrated aqueous HCl (Sigma-Aldrich product number 320331, 12.1 N) in 0.636 mL of acetonitrile was added. The mixture was poured into 29 mm × 10 mm poly(tetrafluoroethylene) molds and allowed to gel overnight in a sealed container with an 1 cm layer of acetonitrile in the bottom to produce an acetonitrile-rich atmosphere. Finally, the pore liquor in the gels was exchanged with pure acetonitrile in preparation for supercritical drying or evaporative drying. Alternatively, according to the method of Pekala et al., 1.98 g of resorcinol, 2.93 g of formaldehyde solution, and 9.65 g of catalyst solution (0.202 g of sodium carbonate dissolved in 100 g of deionized water) were added to 94.24 g deionized water and stirred overnight. Next, the solution was transferred into sealed polypropylene vials which were then placed in an oven at 80 °C for 2−3 days. The resulting RF gels were cut out of the molds with metal-free tools and the pore liquor of the gels was exchanged with pure acetone in preparation for supercritical drying or evaporative drying. RF gels were either supercritically dried from CO_2 to afford an RF aerogel[18] or alternatively evaporatively dried in a sealed container to produce an RF xerogel. Zirconia-containing solutions were then dropcast onto the RF xerogels and aerogels and evaporatively dried. Finally, the zirconia-deposited xerogels and aerogels were pyrolyzed at 800 °C for 10.5 h under a flow of 200 sccm Ar to convert them into four different sample combinations: zirconyl-derived polydisperse nanoparticles on xerogel, monodisperse nanoparticles on xerogel, zirconyl-derived polydisperse nanoparticles on aerogel, and monodisperse nanoparticles on aerogel.

RESULTS

Carbon nanostructures (CNTs and CNFs of varying morphologies) were grown directly on TEM grids and observed with HRTEM. Characterization of nanoparticle catalysts and morphologies of carbon nanostructures were mainly done with lacy-carbon-coated Cu TEM grids, and local characterization of catalyst nanoparticles found Cu does not interact with the growth process. Growths were also performed on metal-free SiN grids, which yielded comparable results, further verifying the observed results were not due to interaction from Cu and validating the local characterization approach on lacy-carbon-coated Cu grids as a means for excluding interactions from Cu (see Supporting Information). After CVD, elongated carbon nanostructures extending from catalyst nanoparticles were consistently observed. Typically, over the majority of the grid, carbon nanostructures attached to zirconia nanoparticles are observed. On the part of the grid where metal nanoparticles were deposited, carbon nanostructures extending from metal nanoparticles attached to zirconia nanoparticle agglomerations are observed. In our experiments, these metal-on-zirconia aggregates represent conventional oxide-supported metal catalysts and serve as a control for comparing nanostructure morphology against metal-free oxide nanoparticles on other parts of the grid. Analysis of nanostructures attached to metal-free oxide nanoparticles were made using nanoparticles located away from the metal-nanoparticle-deposited region of the grid and were verified to be metal-free using lattice fringe analysis and EDX. We observe three types of nanostructure morphologies on our TEM grids, one of which is associated with growth from metal nanoparticles and two of which are associated with growth from zirconia nanoparticles. In the case of growth from oxide-supported metal nanoparticles, a graphitic cage is observed encapsulating the catalyst nanoparticle from which a CNT with approximately the same diameter as the metal nanoparticle extends. We refer to this growth morphology as Type M (for "metallic"). Growth from pure zirconia nanoparticles, however, presents two different morphologies. In some cases, turbostratic CNTs (i.e., hollow tubules with bamboo-like/stacked-cup morphology) are observed extending from zirconia nanoparticles that are two to three times larger in diameter than the CNT (see Figure 1a). We refer to this morphology as Type 1 growth. Unlike oxide-supported metal nanoparticles, no encapsulating graphitic cage is observed around zirconia nanoparticles exhibiting Type 1 growth. Instead, CNTs are found attached to exposed corners of the zirconia nanoparticles as seen in Figure 1b. Closer inspection of the interface between the CNT and zirconia (Figure 1c) reveals a rolled-up graphitic appendage approximately the same diameter as the CNT. This appendage does not encapsulate the zirconia nanoparticle surface but rather is localized as a separate substructure near the nanoparticle corner. The rest of the surface is observed to be covered by few-layer defective carbon domains or remains bare. This localized rolled-up graphitic appendage is consistently found in Type-1 morphology structures as seen in Figures 1, 2, and 3. According to the images of the entire CNT lengths, we conclude that these structures emanate from zirconia nanoparticles via a base growth mechanism (see Figures 1a and 2a). Point-localized EDX spectra taken from the area centering the root of the attached CNT in Figure 1a is shown in Figure 1e. Lattice fringe analysis of zirconia nanoparticles associated with Type 1 growth (see for example Figure 1c) was used to verify nanoparticle composition (note that the Cu peak observed in the EDX spectrum arises from the grid background). No metallic nanoparticles are seen in the vicinity of the zirconia-CNTs structures and so we conclude metal nanoparticles are not responsible for the growth of such CNTs and that the synthesis of these CNTs occurred on a region

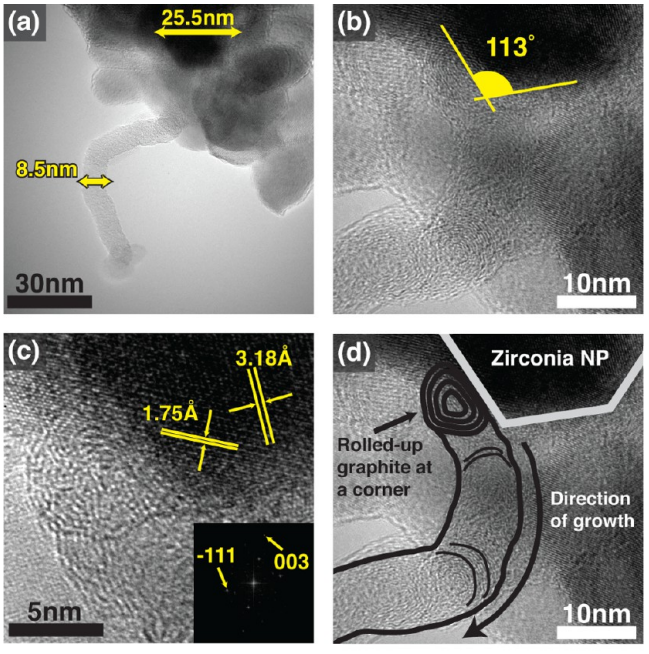

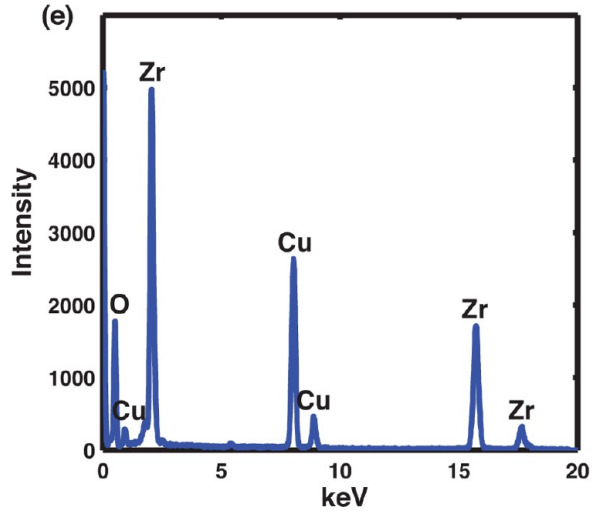

Figure 1. CNT grown from zirconia nanoparticles. (a) A CNT grown from a zirconia nanoparticle catalyst without any other nanoparticles attached on its tip, indicating base-growth. Numbers indicate diameters of the zirconia nanoparticle catalyst and the CNT, 25.5 and 8.5 nm, respectively. (b) A magnified view of the CNT in (a). The CNT is grown from a corner of the zirconia nanoparticle. The number indicates the angle of the corner in degree. (c) A rolled-up graphitic appendage found at the CNT-zirconia nanoparticle interface. The lattice distance and the FFT pattern taken from the nanoparticle validate it to be monoclinic zirconia. (d) Schematic illustration of the Type 1 growth morphology imposed on (b). Information obtained from (c) is reflected on (b). (e) EDX taken from the area centering the root of CNT in (a). The diameter of the electron beam is about 80 nm.

of the zirconia nanoparticle surface. Type 1 growth is only observed at high-angle corners (>110°) of monoclinic zirconia nanoparticles as determined by HRTEM and FFT pattern analysis. Table 1 summarizes the calculated angles between reflections in order to determine whether the nanoparticle attached to the CNTs/CNFs can be assigned to any phase of zirconia. Measured angles are within 5% of error from calculated angles. In order to exclude other compounds and phases, a full list

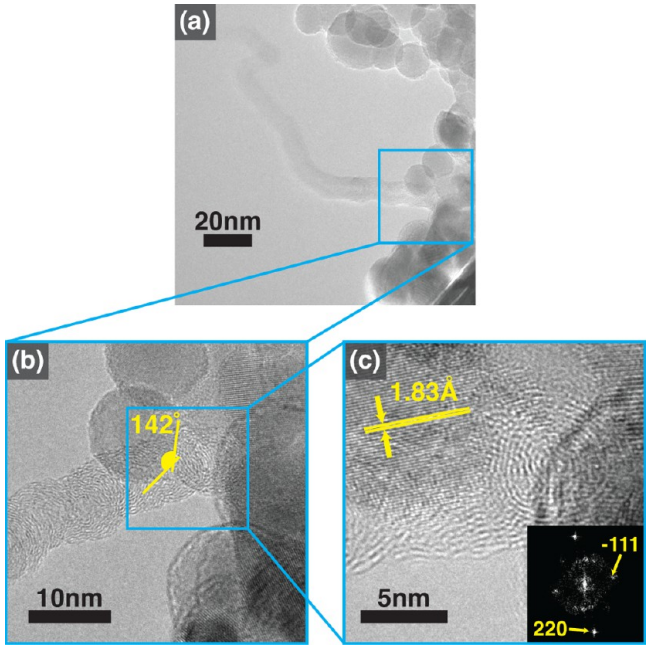

Figure 2. Another example of Type 1 growth of CNT on the corner of zirconia nanoparticles with larger diameter than the CNT itself. (a) A base growth morphology of a CNT extending from a zirconia nanoparticle catalyst. (b) A rolled-up graphite appendage at the interface showing hollow and walls of the CNT. (c) Higher resolution and FFT pattern taken from the nanoparticle validating that the nanoparticle is monoclinic zirconia.

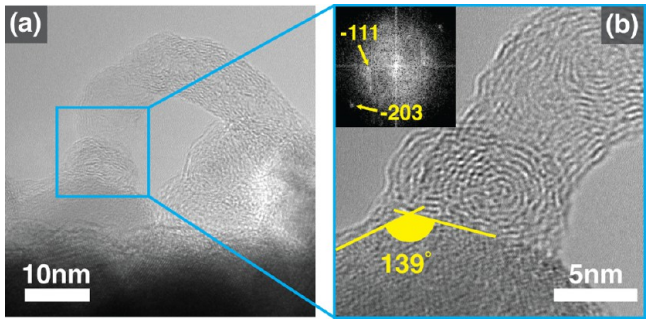

Figure 3. Third example of Type 1 growth of CNT (a) A zirconia nanoparticle catalyst growing a CNT and covered by thin graphitic layer. (b) Higher resolution at the contact between the nanoparticle and the CNT. The FFT pattern taken from the nanoparticle validates the nanoparticle is monoclinic zirconia.

Table 1. List of the FFT Spot Orientation Used to Determine the Phase of Each Nanoparticle Catalyst

possible indices	measured angles between reflections	calculated angles	assigned phases	figure number
{−111}/{003}	117.9°	120.2°	monoclinic	Figure 1c
{−111}/{220}	92.8°	92.7°	monoclinic	Figure 2c
{−111}/{−203}	37.6°	39.4°	monoclinic	Figure 3b
{011}/{101}	68.9°	70.9°	tetragonal	Figure 4c
{011}/{101}	69.9°	70.9°	tetragonal	Figure 5b

of lattice distance and corresponding Miller indices is provided in Table S1.

Aggregated zirconia particles bigger than 50 nm × 50 nm × 100 nm exposing large, flat surfaces are also observed, however

dx.doi.org/10.1021/ja509872y | J. Am. Chem. Soc. 2014, 136, 17808−17817

neither CNTs nor CNFs are seen extending from the middle of such surfaces. This geometric preference toward nanoparticle is consistent with the model of CNT growth from nonmetal nanoparticles previously proposed by Homma et al.,[28] although the morphology observed is not consistent with their representation of graphite lifting off a corner. Figures 2 and 3 are further examples of Type-1 growth. Rolled-up graphitic appendages at the interface between nanostructures and zirconia nanoparticle are again seen, along with either few-layer defective carbon domains or bare surfaces surrounding the nanoparticle. Typical CNTs found exhibiting Type-1 growth were 100 to 200 nm in length. The interface between the rolled-up appendages and the zirconia nanoparticle to which they are attached (Figures 1c, 2c, and 3b) appears to follow the planar surface of the nanoparticle, suggesting that these structures originate on the nanoparticle as opposed to attaching postformation.

The second morphology of carbon nanostructures attached to zirconia nanoparticles observed does not include a rolled-up appendage and is instead characterized by nonhollow nanofibers (CNFs) with approximately the same diameter as the zirconia catalyst nanoparticle. We refer to this morphology as Type 2 growth, and Figure 4 represents it. In this type of growth,

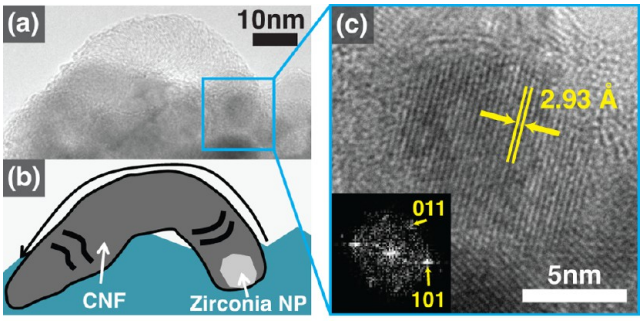

Figure 4. Type 2 growth from zirconia nanoparticle (a) A CNF growing from a zirconia nanoparticle with a comparable diameter. (b) Schematic illustration of (a). A black arrow indicates the direction of growth. (c) A high magnification view of the catalytic zirconia nanoparticle. The nanoparticle is buried in the zirconia nanoparticle aggregates. Faceted shape is observed. FFT pattern validates the nanoparticle is tetragonal zirconia.

multiple individual CNFs extending from different zirconia nanoparticles may merge into larger structures. Figure 5a and 5b

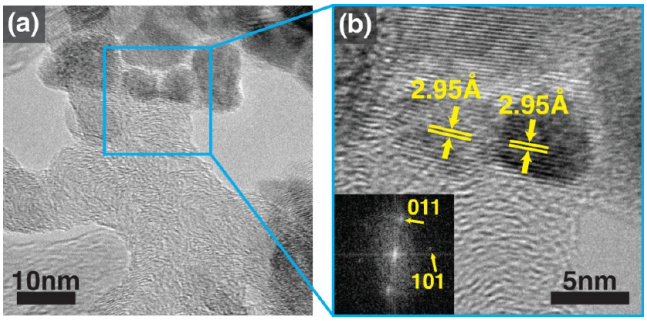

Figure 5. Examples of merging carbon nanostructures synthesized by multiple zirconia nanoparticle catalysts. (a) CNFs grown from two adjacent zirconia nanoparticles and fused together. (b) A high magnification view of the zirconia nanoparticles growing CNFs. FFT pattern is taken from the right zirconia nanoparticle and shows that the nanoparticle is tetragonal zirconia.

show an example of how multiple zirconia-attached CNFs may fuse into a larger-diameter nanostructure. In these examples, nanostructures are observed extending from isolated particles while continuous conformal turbostratic carbon layers are observed following the contour surfaces of aggregates of multiple zirconia particles. Those turbostratic carbon layers are thinner than the graphitic cage seen around metallic nanoparticle catalysts.

On the region of the TEM grids where metal nanoparticles were placed through controlled contact with a stainless steel instrument, CNTs attached to metal (Cr and Fe) nanoparticles are observed exhibiting Type M growth. Figure 6a and 6b show a CNT grown from an Cr nanoparticle and Figure 6c shows a CNT grown from Fe nanoparticle. A graphitic cage is observed surrounding those metal nanoparticles. Additionally, metal nanoparticle catalysts are occasionally seen protruding into the hollow length of the attached CNT as seen in Figure 6c, which has not been seen with Type 1 nor Type 2 growth at all. Fe and Cr nanoparticles are consistently found with a graphitic cage that is thicker than the thin carbon layers found covering zirconia nanoparticle catalysts. These morphologies indicate that with the conditions employed in this work the Type M growth is independent of zirconia on which the metal nanoparticles are placed, unlike the cases that both metal nanoparticles and metal oxide supports are involved.[46] We note that the TEM grids used in this work were comprised of Cu and that Cu nanoparticles have also been reported to serve as catalysts for CVD growth of CNTs.[47] However, only on rare occasions were Cu nanoparticles observed on the TEM grids and thus are generally believed to not have contributed to nanostructure growth. As discussed later, potential contribution from Cu was excluded by comparable growth on metal-free SiN TEM grids.

DISCUSSION

We start discussion with differences observed between carbon nanostructure growth resulting from zirconia nanoparticles and metal nanoparticles. Table 2 summarizes our observations of the nanostructure morphologies found under HRTEM in this study and features observed for metallic vs zirconia nanoparticle catalysts studied in this work. A schematic representation of Type 1, Type 2, and Type M growth are depicted in Figure 7. A graphitic multilayered cage is not observed for oxide nanoparticles (Type 1 or Type 2 growth), while it is always observed for metal nanoparticles (Type M growth). Instead, thin, defect-rich graphitic layers on the exposed surfaces of zirconia nanoparticles are occasionally observed. The interface between two or more zirconia nanoparticles aggregated together does not have such layers (see Figure 6b). After annealing TEM grid dropcast with catalyst precursors, before CVD, also exhibit nanoparticles with similar thin graphitic layers, consistent with the previously reported propensity for zirconia nanoparticles to graphitize amorphous carbon at elevated temperatures.[9] Therefore, we conclude that these thin graphitic layer domains are due to solid-state rearrangement of amorphous carbon either from lacy carbon or by decomposing carbon feedstock by zirconia nanoparticles[48] and not precipitation of carbon from oversaturated zirconia-carbon solid solutions (as is observed in some cases for metal nanoparticle catalysts).

Contact between carbon nanostructures and nanoparticle catalysts is another notable difference between Type M and oxide-based growth. In Type M growth, carbon atoms near metal nanoparticle catalysts appear to be templated into a continuous graphitic cage surrounding the entire metal nanoparticle catalyst.

dx.doi.org/10.1021/ja509872y | J. Am. Chem. Soc. 2014, 136, 17808−17817

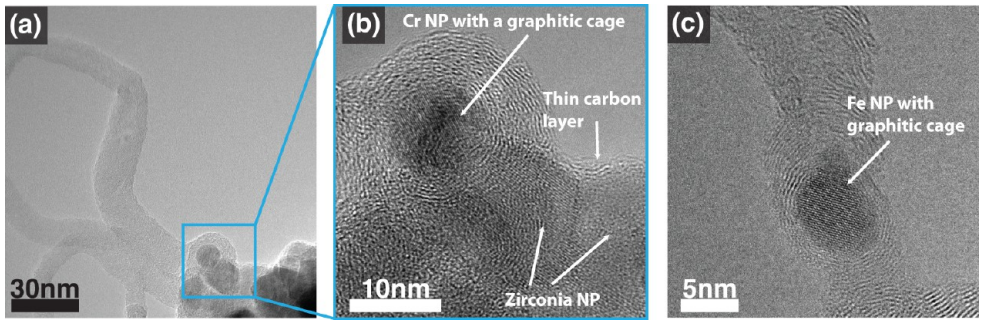

Figure 6. CNT Growth from metals observed in this work. (a) A Cr nanoparticle adjacent to zirconia nanoparticles. Only the Cr nanoparticle is growing CNT. (b) A high magnification view of the Cr and zirconia nanoparticles in (a). The graphitic cage around the Cr nanoparticle is much thicker than the carbon layer on zirconia nanoparticles. Such carbon layer deposits only on the exposed surface of zirconia nanoparticles, not on the interface of zirconia nanoparticles aggregated together, indicating the layers are not formed by precipitation of carbon from zirconia nanoparticle saturated with carbon. (c) A Fe nanoparticle growing CNT. Thick graphitic cage and projection of Fe nanoparticle into CNT hollow is observed.

Table 2. Characterization of Nanostructure Growths Observed in the Present Work

	zirconia Type 1	zirconia Type 2	metal nanoparticles
carbon around nanoparticle	rolled-up graphite and thin graphitic layer	thin graphitic layer	graphitic cage
nanoparticle diameter (D_{np})	10 to 30 nm	5 to 10 nm	5 to 10 nm
nanostructure diameter (D_f)	5 to 10 nm	5 to 10 nm	5 to 10 nm
D_{np}/D_f	2 to 3	1	1
nanostructure−catalyst interface	corner	corner	all around
nanoparticle phase	monoclinic	tetragonal	−
nanostructure type	turbostratic CNT	turbostratic CNF	turbostratic CNT

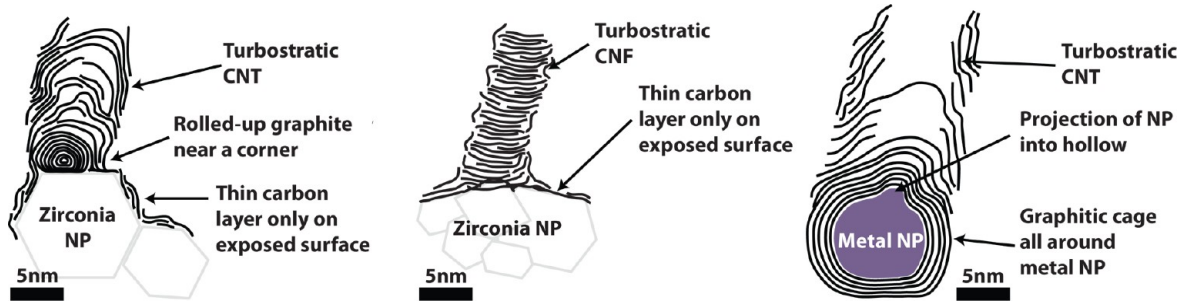

Figure 7. Schematic illustrations of Type 1 growth morphology for zirconia nanoparticles (left), Type 2 growth morphology for zirconia nanoparticles (middle), and Type M growth morphology for metal nanoparticles (right).

In Type 1 and Type 2 oxide growth on the other hand, zirconia nanoparticles are attached to the elongated carbon nanostructure only at the surface exposed to gas flow. As mentioned, when CNTs rather than CNFs result from oxides (Type 1 growth), a rolled-up graphitic appendage near a high angle corner of zirconia nanoparticles is observed. Carbon nanoonions, a related carbon nanostructure, are usually synthesized by pyrolysis using metal catalysts at high temperatures ranging from 900 to 1200 °C[49,50] and as low as 750 °C using Co metal as catalyst.[51] Energetic agitation or a catalyst is typically needed to form carbon nanoonions, indicating a high activation energy of the reaction. Catalyst-synthesized carbon nanoonions are also turbostratic and similar to the rolled-up graphitic appendages observed in this work. Therefore, we conclude that zirconia nanoparticles are catalytically active at their surfaces within a vicinity of a high-angle corner. These features are evidence that the growth process of carbon nanostructures from zirconia nanoparticle catalysts is surface-bound and different from the dissolution-based mechanism of growth seen with metallic nanoparticle catalysts.[52−54] This is consistent with the expected stability of zirconia nanoparticles arising from the high melting point of zirconia and low diffusivity of carbon atoms in zirconia at the reaction temperatures considered here.[27] Additionally, no zirconia nanoparticle catalyst associated with carbon nanostructure growth contain phases assigned to zirconium carbide as determined by lattice fringe and FFT pattern analysis, which further supports that there has not been significant dissolution of carbon atoms into the zirconia nanoparticles. These two differences in morphology as observed in this work also suggest why zirconia nanoparticles have not been able to show growth yield as high as popular metal nanoparticles do, especially for hollow carbon nanostructures (CNTs) observed in Type 1 and Type M growth: we believe a defective, spherical, graphitic template (e.g., nanoonion or cage) may be necessary in order to direct amorphous carbon into curved graphite rather than flat graphite and to facilitate incorporation of carbon atoms into a growing hollow nanostructure. Metal nanoparticles can serve as such a spherical object, since dissolution of carbon atoms into the metal nanoparticle followed by precipitation of carbon forms the needed graphitic cage that follows the spherical shape of the nanoparticle. The free energy of the system decreases accordingly, enabling nucleation and growth of the CNT to

dx.doi.org/10.1021/ja509872y | J. Am. Chem. Soc. 2014, 136, 17808−17817

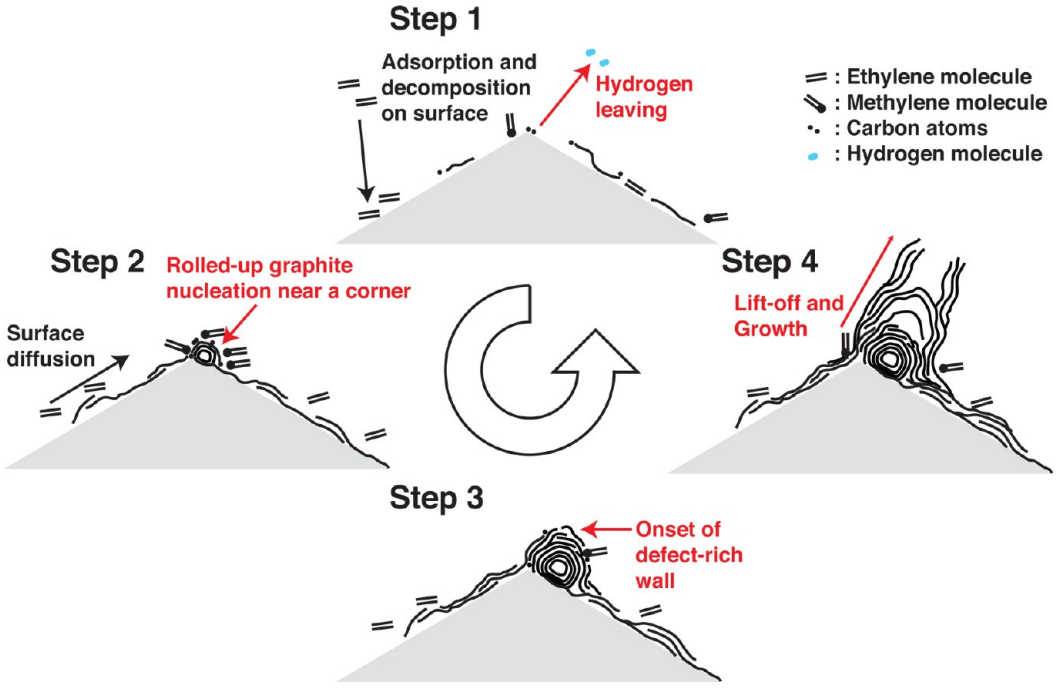

Figure 8. Description of the proposed Type 1 growth model.

occur spontaneously as carbon concentration in the metal nanoparticles reaches the solubility limit.[55,56] Zirconia nanoparticles, on the other hand, have to develop a rolled-up appendage to serve as a graphitic template in order for CNT growth to occur. Indeed, as seen in the upper part of Figure 2a, we observe zirconia nanoparticles that are partially covered by thin graphitic layers but without a rolled-up graphitic appendage and these nanoparticles do not produce CNTs or CNFs. We conclude that formation of a rolled-up graphitic appendage, which appears to occur at corners of zirconia nanoparticles, is a statistical and high-activation-energy process, translating into lower CNT growth yields when compared to CNT growth with metals.

On the basis of the morphological differences observed in this work, we suggest a growth model of hollow carbon nanostructures (such as turbostratic CNTs) grown from zirconia nanoparticle catalysts as follows (see Figure 8). First, adsorption of ethylene molecules occurs over the zirconia nanoparticle surface, as shown in Step 1 of Figure 8. The ethylene molecules may develop thin carbon layers not as thick as seen with Type M growth or may desorb before decomposition (e.g., hydrogenation). A certain amount of the adsorbed ethylene molecules that diffuse over the surface and find chemisorption cites eventually decompose into carbon atoms or other fundamental structural unit (e.g., methylene). Such sites are more often found near a corner which is richer in kinks and are most likely zirconium cation sites.[57] Then near the corner a dense carbon atom cluster is formed, which eventually transforms into a nascent rolled-up graphite. Step 2 of Figure 8 describes this process. Carbon atoms then accumulate, rolling into a rolled-up graphitic appendage by further surface diffusion and concurrent decomposition of feedstock molecules. Initially incorporating carbon atoms to extend rolled-up graphite would be the rate limiting step because of high free energy associated with high curvature. At this point, diffusion and decomposition processes would supply a sufficient number of carbon atoms to develop a graphitic shell. As the rolled-up graphitic appendage grows, incorporation of carbon atoms accelerates because of the resulting lower curvature that in turn reduces the activation energy of incorporating additional carbon atoms. Increasingly more carbon atoms are then required to provide each subsequent layer of the growing rolled-up graphitic appendage, and diffusion and/or decomposition of feedstock molecules becomes the limiting step in growth of the structure. As a result, each next shell becomes increasingly likely to have defects. Step 3 of Figure 8 depicts how this type of structure may look. The outermost shell would consist of multiple graphitic patches, so eventually a portion of the shell lifts off[58] as spacing between layers in a carbon nanoonion increases[59] and thus interlayer binding force decreases. The appendage would not grow larger spherically, but rather a hollow carbon nanostructures, namely turbostratic CNTs, would start to grow (Step 4 of Figure 8). We observe an intermediate structure consistent with our model. Figure 9 shows a zirconia nanoparticle with a thin graphitic layer surrounding it. Near a high-angle corner of the zirconia nanoparticle (yellow arrow), a nascent carbon nanoonion is observed, which we feel represents a state between Steps 2 and 3 of Figure 8.

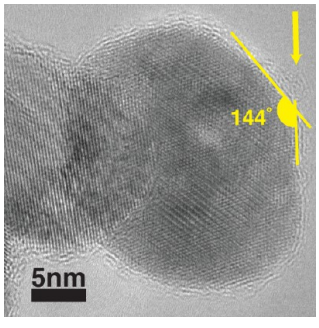

Figure 9. A prospective intermediate state for Type 1 growth (see step 2 and 3 in Figure 8). The yellow arrow indicates nucleation of rolled-up graphite near a high angle corner.

dx.doi.org/10.1021/ja509872y | J. Am. Chem. Soc. 2014, 136, 17808−17817

Carbon nanostructures from both Type 1 and 2 growth are composed of defect-rich (turbostratic) graphite. Even though smaller zirconia nanoparticles as those that appear to facilitate Type 2 growth do not grow hollow nanostructures (apparently due to their lack of associated rolled-up graphitic appendage), they are still active catalysts for both graphitization of amorphous carbon and growth of graphitic nanofibers. The size and edge angles of zirconia nanoparticles, rather than phase, seems to be responsible for the propensity of a zirconia nanoparticle to form an appendage. This suggests that dispersion and annealing of zirconia nanoparticle precursors on porous carbonaceous substrates could result in a higher population of prestructures for either Type 1 or Type 2 growth morphology. Steiner III et al. demonstrated that zirconia nanoparticles are effective catalysts for solid-state graphitization of amorphous carbon.[9] They observed that pyrolysis of zirconyl-doped resorcinol-formaldehyde-type polymer aerogels produces zirconia nanoparticles encapsulated in cage-like fullerenic nanostructures.[9] The caged zirconia nanoparticles exhibit similar diameters to zirconia nanoparticles that result in Type-2 growth in this study (Figure 4 and 5). In this case three reactions occur concurrently: (1) carbothermal reduction of polymer-bound zirconyl ions to zirconia nanoparticles; (2) pyrolysis of RF polymer into amorphous carbon; and (3) solid-state catalytic conversion of the resulting amorphous carbon into graphitic nanostructures by zirconia nanoparticles. In our experiments the zirconia nanoparticles synthesized on lacy carbon were mostly larger in size and did not initially develop fullerenic cages. Contextualizing the observations of Steiner III et al. through our model, we hypothesize that pretreatment of zirconia nanoparticles with solid and highly porous carbon would result in well dispersed, appropriately sized zirconia nanoparticles surrounded by graphitic carbon matrix that would be active toward CNT growth, and thus serve as a means for enhancing the activity of zirconia toward CNT growth.

To test this hypothesis, we evaluated the effect of pyrolyzing two types of zirconia nanoparticle catalysts (monodisperse 4 nm-diameter monoclinic zirconia nanoparticles prepared according to the method of Joo et al.[33] and polydisperse zirconia nanoparticles from solutions of zirconium oxychloride in isopropanol prepared according to the method of Steiner III et al.[9]) on high-surface-area carbonizable substrates (resorcinol-formaldehyde polymer aerogels, ($\Pi \geq 95\%$) and xerogels, ($\Pi \sim 10\%$)) and then performing CVD growth with the pyrolyzed substrates.

Both types of substrates are of defect-rich graphitic material[60,61] so potentially grow CNTs by themselves.[62] However, dropcasting zirconia precursor solution was expected to substantially increase the number of active spots toward nanostructure growth present in the materials. Following CVD, very sporadic CNT growth bundles may be found on the surfaces of both types of the substrates without zirconia (Figure 10a,b). Aerogels and xerogels with zirconia nanoparticles, however, exhibit substantial nanostructure growth (Figures 10c–f) on the regions of the substrates where monodisperse zirconia nanoparticle solution or zirconium oxychloride solution was applied. Carbon aerogel and xerogel substrates dropcast with either source of zirconia yielded elongated nanostructure growth spanning ranges of the surface, especially edges of the substrates—nanostructure growth that is not observed on the surface of the control samples, which only present individual bundles at best (Figure 10a,b). A clear dependence of nanostructure diameter and length on the zirconia source is

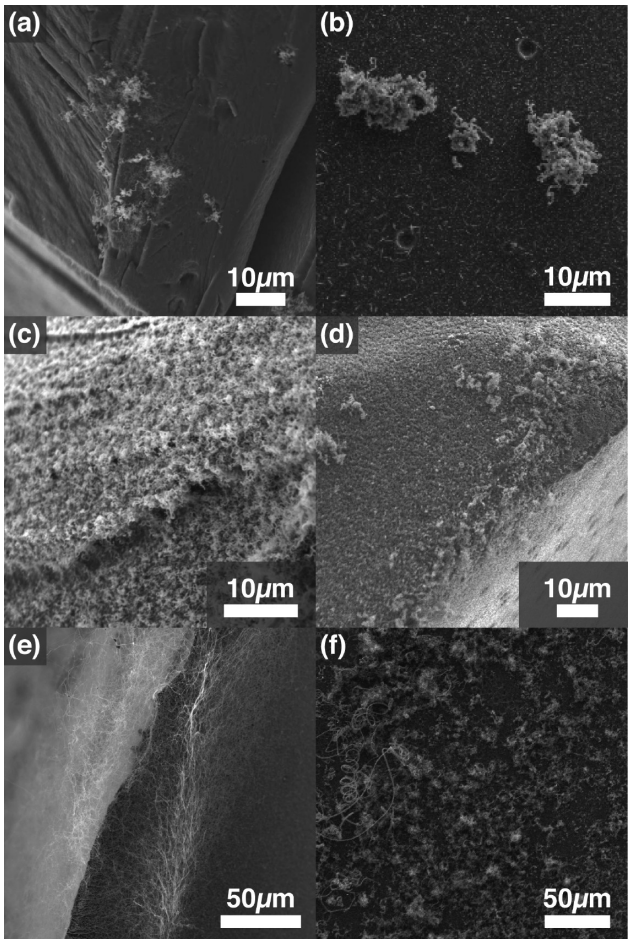

Figure 10. Representative growth morphologies obtained with carbon aerogel and xerogel substrates. (a) Carbon aerogel without catalyst solution. (b) Carbon xerogel without catalyst solution. (c) Carbon aerogel with prefabricated zirconia nanoparticle solution. (d) Carbon xerogel with prefabricated zirconia nanoparticle solution. (e) Carbon aerogel with zirconia oxychloride octahydrate solution. (f) Carbon xerogel with zirconia oxychloride octahydrate solution.

observed with aerogel substrates: substrates dropcast with zirconium oxychloride resulted in finer, longer nanostructures, whereas substrates dropcast with prefabricated zirconia nanoparticles resulted in thicker, shorter nanostructures sprouting over various areas of the substrate. It is believed that the two different zirconia sources distinguishably affect the diameter and length of the nanostructures that form, as substrates containing the monodisperse prefabricated nanoparticles would be expected to undergo a greater degree of zirconia nanoparticle coarsening than those dropcast with solution-phase monomeric precursor, resulting in larger zirconia particle size and thus larger diameter of grown nanostructures. On carbon xerogel substrates, zirconia nanoparticles derived from zirconia oxychloride octahydrate showed impressively enhanced growth yield compared to control samples. The growth comprises a polydisperse variety of elongated carbon nanostructures, both thin and thick as well as long and short. Dispersion of prefabricated zirconia nanoparticles on xerogels showed a large number of short-length bundles and even higher on carbon aerogel substrates. We submit that the high porosity and surface area of the aerogel substrate facilitates finer dispersion and therefore more efficient progression of the reactions required for solid-state graphitization of the aerogel's amorphous carbon framework into graphitic

carbon. The higher yields observed when using zirconium oxychloride solution, which contains molecularly dispersed zirconyl ions as well as fine diameter nanoparticles, suggests that smaller particles afford longer lengths and higher yields than larger or agglomerated particles with carbon gel substrates. In summary, we have found that pyrolytic pretreatment of zirconia nanoparticles with solid-state amorphous carbon is a viable method for activating such particles for CVD growth of CNTs/CNFs, which is a result of solid-state catalytic graphitization of surrounding amorphous carbon. TEM imaging revealed these fibrils to be a mixture of turbostratic CNTs and CNFs, i.e., a mixture of Type-1 and Type-2 growth from zirconia nanoparticles. We note that TEM samples of those CNTs/CNFs grown on these 3D substrates largely showed fibrils without zirconia nanoparticles attached, that is, the fibrils were separated from the catalysts from which they grew. This supports the observation that the zirconia nanoparticles in these substrates are surrounded by solid-state graphitic carbon, which anchors them into the substrate more firmly than the fibrils are attached to the nanoparticles. We also note that the crystallinity of these CNTs is relatively lower than those previously reported with zirconia nanoparticles,[9] indicative of changes in CVD parameters used (e.g., gas pressure and carbon feedstock species) that should affect CNT/CNF growth by zirconia nanoparticle catalysts.

We further explored whether metal adatoms may play a role in the growth observations by growing on metal-free substrates, namely, SiN and SiN coated with pyrolytic carbon. As seen in Figure S1, we observe Type-1 growth from zirconia nanoparticles on SiN grids. Similar growth is observed on pyrolytic-carbon-coated SiN grid (see Figures S2 and S3). In addition, we see clearly that an isolated zirconia nanoparticle grows CNTs as in Figure S4. These studies on SiN TEM grids indicate that neither the spatially separated control metal nanoparticles nor the Cu grid on the Cu TEM grids determine nanostructure and that rather the growth is due to zirconia nanoparticles. Recently, morphologies of carbon nanostructures similar to those investigated in this work have been reported in solid oxide fuel cells (SOFCs) comprised of yttria-stabilized zirconia.[63,64]

■ CONCLUSION

Distinct differences in the morphologies of carbon nanostructures resulting from CVD growth employing zirconia nanoparticle catalysts and metal nanoparticle catalysts are observed. Lattice-fringe resolved HRTEM and FFT pattern analysis unambiguously show that zirconia nanoparticles, varying in shape and phase, grow both hollow and nonhollow fibrous carbon nanostructures without interactions with metals including Cu from lacy-carbon-coated Cu TEM grids. We observe two nanostructure growth morphologies associated with zirconia nanoparticle catalysts: growth of hollow carbon nanostructures with a rolled-up graphitic appendage on a high-angle corner of the nanoparticle smaller in diameter than the parent nanoparticle (termed Type 1 growth), and growth of nonhollow carbon nanofibers approximately the same in diameter as the nanoparticle (termed Type 2 growth). In both cases, no substantial graphitic cage encapsulating the oxide nanoparticle catalyst is observed, where a cage is almost always observed with metal nanoparticle catalysts (termed Type M growth). On the basis of these observations, a growth model for zirconia nanoparticle catalysts is proposed. We explain the lower growth yield from zirconia nanoparticles compared to metal nanoparticles by the high activation energy required to form a rolled-up graphitic appendage at zirconia nanoparticle corners. We further demonstrate a practical method for achieving high-yield CVD growth of CNTs and CNFs with zirconia nanoparticles that exploits the mechanistic insights of our growth model. These insights are expected to extend to other nonmetallic nanoparticle growth catalysts and enable applications using CNTs that are hindered by the presence of residual metal catalysts.

■ ASSOCIATED CONTENT

Supporting Information

A full list of lattice distance and corresponding Miller indices used for FFT pattern analysis and Cs-corrected HRTEM images with EDX spectrum for samples synthesized on SiN TEM grids. This material is available free of charge via the Internet at http://pubs.acs.org.

■ AUTHOR INFORMATION

Corresponding Author

wardle@mit.edu

Notes

The authors declare no competing financial interest.

■ ACKNOWLEDGMENTS

This material is based upon work supported by the National Science Foundation under Grant No. 1007793 and was also supported by Airbus group, Boeing, Embraer, Lockheed Martin, Saab AB, Hexcel, and TohoTenax through MIT's Nano-Engineered Composite aerospace STructures (NECST) Consortium. This research was supported (in part) by the U.S. Army Research Office under Contract W911NF-13-D-0001. This work was performed in part at the Center for Nanoscale Systems (CNS), a member of the National Nanotechnology Infrastructure Network (NNIN), which is supported by the National Science Foundation under NSF Award No. ECS-0335765. CNS is part of Harvard University. This work was carried out in part through the use of MIT Microsystems Technology Laboratories. Stephan Hofmann acknowledges funding from EPSRC under grant EP/H047565/1. Piran Kidambi acknowledges the Lindemann Trust Fellowship. The authors thank Prof. Taeghwan Hyeon and Jaewon Moon at Seoul National University for synthesizing zirconia nanoparticles.

■ REFERENCES

(1) Li, Y.-L.; Kinloch, I. A.; Windle, A. H. *Science* **2004**, *304*, 276−278.
(2) Dalton, A. B.; Collins, S.; Munoz, E.; Razal, J. M.; Ebron, V. H.; Ferraris, J. P.; Coleman, J. N.; Kim, B. G.; Baughman, R. H. *Nature* **2003**, *423*, 703−703.
(3) Shulaker, M. M.; Hills, G.; Patil, N.; Wei, H.; Chen, H.-Y.; Wong, H.-S. P.; Mitra, S. *Nature* **2013**, *501*, 526−530.
(4) Tans, S. J.; Verschueren, A. R. M.; Dekker, C. *Nature* **1998**, *393*, 49−52.
(5) Yi, H.; Ghosh, D.; Ham, M.-H.; Qi, J.; Barone, P. W.; Strano, M. S.; Belcher, A. M. *Nano Lett.* **2012**, *12*, 1176−1183.
(6) Rummeli, M.; Kramberger, C.; Gruneis, A.; Ayala, P.; Gemming, T.; Buchner, B.; Pichler, T. *Chem. Mater.* **2007**, *19*, 4105.
(7) Rummeli, M.; Bachmatiuk, A.; Borrnert, F.; Schaffel, F.; Ibrahim, I.; Cendrowski, K.; Simha-Martynkova, G.; Placha, D.; Borowiak-Palen, E.; Cuniberti, G.; Buchner, B. *Nanoscale Res. Lett.* **2011**, *6*, 303.
(8) Lin, J.-H.; Chen, C.-S.; Ma, H.-L.; Chang, C.-W.; Hsu, C.-Y.; Chen, H.-W. *Carbon* **2008**, *46*, 1619−1623.
(9) Steiner, S.; Baumann, T.; Bayer, B.; Blume, R.; Worsley, M.; MoberlyChan, W.; Shaw, E.; Schlogl, R.; Hart, A.; Hofmann, S.; Wardle, B. *J. Am. Chem. Soc.* **2009**, *131*, 12144.
(10) Liu, H.; Takagi, D.; Ohno, H.; Chiashi, S.; Chokan, T.; Homma, Y. *Appl. Phys. Express* **2008**, *1*, 014001.

(11) Cai, Q.; Hu, Y.; Liu, Y.; Huang, S. *Appl. Surf. Sci.* **2012**, *258*, 8019−8025.
(12) Bayer, B. C.; Castellarin-Cudia, C.; Blume, R.; Steiner, S. A.; Ducati, C.; Chu, D.; Goldoni, A.; Knop-Gericke, A.; Schlogl, R.; Cepek, C.; Robertson, J.; Hofmann, S. *RSC Adv.* **2013**, *3*, 4086−4092.
(13) Liu, B.; Ren, W.; Gao, L.; Li, S.; Pei, S.; Liu, C.; Jiang, C.; Cheng, H.-M. *J. Am. Chem. Soc.* **2009**, *131*, 2082.
(14) Takagi, D.; Hibino, H.; Suzuki, S.; Kobayashi, Y.; Homma, Y. *Nano Lett.* **2007**, *7*, 2272.
(15) Takagi, D.; Kobayashi, Y.; Homma, Y. *J. Am. Chem. Soc.* **2009**, *131*, 6922.
(16) Qian, H.; Greenhalgh, E. S.; Shaffer, M. S. P.; Bismarck, A. *J. Mater. Chem.* **2010**, *20*, 4751−4762.
(17) Reddy, A. L. M.; Shaijumon, M. M.; Gowda, S. R.; Ajayan, P. M. *Nano Lett.* **2009**, *9*, 1002−1006.
(18) Steiner, S. A. Ph.D. Thesis, Massachusetts Institute of Technology, Cambridge, MA, 2012.
(19) Tan, L.-L.; Ong, W.-J.; Chai, S.-P.; Mohamed, A. R. *Catal. Today* **2013**, *217*, 1−12.
(20) Plata, D. L.; Meshot, E. R.; Reddy, C. M.; Hart, A. J.; Gschwend, P. M. *ACS Nano* **2010**, *4*, 7185−7192.
(21) Hofmann, S.; et al. *Nano Lett.* **2007**, *7*, 602−608.
(22) Kukovitsky, E.; L'vov, S.; Sainov, N. *Chem. Phys. Lett.* **2000**, *317*, 65−70.
(23) Ogrin, D.; Colorado, R., Jr.; Maruyama, B.; Pender, M. J.; Smalley, R. E.; Barron, A. R. *Dalton Trans.* **2006**, 229−236.
(24) Yoshida, H.; Takeda, S.; Uchiyama, T.; Kohno, H.; Homma, Y. *Nano Lett.* **2008**, *8*, 2082−2086. PMID: 18505300
(25) Wirth, C. T.; Bayer, B. C.; Gamalski, A. D.; Esconjauregui, S.; Weatherup, R. S.; Ducati, C.; Baehtz, C.; Robertson, J.; Hofmann, S. *Chem. Mater.* **2012**, *24*, 4633−4640.
(26) Steiner, S. A. Master Thesis, Massachusetts Institute of Technology, Cambridge, MA, 2006.
(27) Vykhodets, V.; Kurennykh, T.; Kesarev, A.; Kuznetsov, M.; Kondrat'ev, V.; Hülsen, C.; Koester, U. *JETP Lett.* **2011**, *93*, 5−9.
(28) Homma, Y.; Liu, H.; Takagi, D.; Kobayashi, Y. *Nano Res.* **2009**, *2*, 793−799.
(29) Noda, S.; Hasegawa, K.; Sugime, H.; Kakehi, K.; Zhang, Z.; Maruyama, S.; Yamaguchi, Y. *Jpn. J. Appl. Phys.* **2007**, *46*, L399−L401.
(30) Mattevi, C.; Wirth, C. T.; Hofmann, S.; Blume, R.; Cantoro, M.; Ducati, C.; Cepek, C.; Knop-Gericke, A.; Milne, S.; Castellarin-Cudia, C.; Dolafi, S.; Goldoni, A.; Schloegl, R.; Robertson, J. *J. Phys. Chem. C* **2008**, *112*, 12207−12213.
(31) Magrez, A.; Smajda, R.; Seo, J. W.; Horváth, E.; Rebernik, R. P.; Andresen, J. C.; Acquaviva, D.; Olariu, A.; Laurenczy, G.; Forró, L. *ACS Nano* **2011**, *5*, 3428−3437.
(32) Liu, B.; Tang, D.-M.; Sun, C.; Liu, C.; Ren, W.; Li, F.; Yu, W.-J.; Yin, L.-C.; Zhang, L.; Jiang, C.; Cheng, H.-M. *J. Am. Chem. Soc.* **2011**, *133*, 197−199.
(33) Joo, J.; Yu, T.; Kim, Y. W.; Park, H. M.; Wu, F.; Zhang, J. Z.; Hyeon, T. *J. Am. Chem. Soc.* **2003**, *125*, 6553−6557.
(34) Winterer, M.; Delaplane, R.; McGreevy, R. *J. Appl. Crystallogr.* **2002**, *35*, 434−442.
(35) Chen, L.; Mashimo, T.; Omurzak, E.; Okudera, H.; Iwamoto, C.; Yoshiasa, A. *J. Phys. Chem. C* **2011**, *115*, 9370−9375.
(36) Srinivasan, R.; De Angelis, R. J.; Ice, G.; Davis, B. H. *J. Mater. Res.* **1991**, *6*, 1287−1292.
(37) Silva, G. C.; Kercher, A. A.; Hunn, J. D.; Martin, R. C.; Jellison, G. E.; Meyer, H. M. *J. Solid State Chem.* **2012**, *194*, 91−99.
(38) Goldak, J.; Lloyd, L. T.; Barrett, C. S. *Phys. Rev.* **1966**, *144*, 478−484.
(39) Wilman, H.; Sinha, A. B. P. *Acta Crystallogr.* **1954**, *7*, 682.
(40) Straumanis, M. E.; Weng, C. C. *Acta Crystallogr.* **1955**, *8*, 367−371.
(41) Straumanis, M. E.; Yu, L. S. *Acta Crystallogr., Sect. A: Cryst. Phys., Diffr., Theor. Gen. Crystallogr.* **1969**, *25*, 676−682.
(42) Golden, T. D.; Shumsky, M. G.; Zhou, Y.; VanderWerf, R. A.; Van Leeuwen, R. A.; Switzer, J. A. *Chem. Mater.* **1996**, *8*, 2499−2504.
(43) Forsyth, J. B.; Hull, S. *J. Phys.: Condens. Matter* **1991**, *3*, 5257.
(44) Mulik, S.; Sotiriou-Leventis, C.; Leventis, N. *Chem. Mater.* **2007**, *19*, 6138−6144.
(45) Pekala, R. W.; Alviso, C. T. *MRS Online Proc. Libr.* **1992**, DOI: 10.1557/PROC-270-3.
(46) Rümmeli, M. H.; Schäffel, F.; Kramberger, C.; Gemming, T.; Bachmatiuk, A.; Kalenczuk, R. J.; Rellinghaus, B.; Büchner, B.; Pichler, T. *J. Am. Chem. Soc.* **2007**, *129*, 15772−15773.
(47) Takagi, D.; Kobayashi, Y.; Hibino, H.; Suzuki, S.; Homma, Y. *Nano Lett.* **2008**, *8*, 832.
(48) Kidambi, P. R.; Bayer, B. C.; Weatherup, R. S.; Ochs, R.; Ducati, C.; Szabó, D. V.; Hofmann, S. *Phys. Status Solidi RRL* **2011**, *5*, 341−343.
(49) Jin, Y. Z.; Gao, C.; Hsu, W. K.; Zhu, Y.; Huczko, A.; Bystrzejewski, M.; Roe, M.; Lee, C. Y.; Acquah, S.; Kroto, H.; Walton, D. R. *Carbon* **2005**, *43*, 1944−1953.
(50) Serp, P.; Feurer, R.; Kalck, P.; Kihn, Y.; Faria, J.; Figueiredo, J. *Carbon* **2001**, *39*, 621−626.
(51) Xu, Z.-X.; Lin, J.-D.; Roy, V.; Ou, Y.; Liao, D.-W. *Mater. Sci. Eng., B* **2005**, *123*, 102−106.
(52) Klinke, C.; Bonard, J.-M.; Kern, K. *Phys. Rev. B: Condens. Matter Mater. Phys.* **2005**, *71*, 035403.
(53) Chhowalla, M.; Teo, K. B. K.; Ducati, C.; Rupesinghe, N. L.; Amaratunga, G. A. J.; Ferrari, A. C.; Roy, D.; Robertson, J.; Milne, W. I. *J. Appl. Phys.* **2001**, *90*, 5308−5317.
(54) Diarra, M.; Zappelli, A.; Amara, H.; Ducastelle, F.; Bichara, C. *Phys. Rev. Lett.* **2012**, *109*, 185501.
(55) Deck, C. P.; Vecchio, K. *Carbon* **2006**, *44*, 267−275.
(56) Ding, F.; Rosén, A.; Bolton, K. *J. Chem. Phys.* **2004**, *121*, 2775−2779.
(57) Busca, G.; Lorenzelli, V.; Ramis, G.; Saussey, J.; Lavalley, J. *J. Mol. Struct.* **1992**, *267*, 315−329.
(58) Schebarchov, D.; Hendy, S. C.; Ertekin, E.; Grossman, J. C. *Phys. Rev. Lett.* **2011**, *107*, 185503.
(59) Gan, Y.; Banhart, F. *Adv. Mater.* **2008**, *20*, 4751−4754.
(60) Alegre, C.; Sebastián, D.; Baquedano, E.; Gálvez, M. E.; Moliner, R.; Lázaro, M. J. *Catalysts* **2012**, *2*, 466−489.
(61) Reynolds, G.; Fung, A.; Wang, Z.; Dresselhaus, M.; Pekala, R. *J. Non-Cryst. Solids* **1995**, *188*, 27−33.
(62) Lin, J. H.; Chen, C. S.; Rümmeli, M. H.; Bachmatiuk, A.; Zeng, Z. Y.; Ma, H. L.; Büchner, B.; Chen, H. W. *Chem. Mater.* **2011**, *23*, 1637−1639.
(63) Kogler, M.; Köck, E.-M.; Perfler, L.; Bielz, T.; Stöger-Pollach, M.; Hetaba, W.; Willinger, M.; Huang, X.; Schuster, M.; Klötzer, B.; Penner, S. *Chem. Mater.* **2014**, *26*, 1690−1701.
(64) Tao, Y.; Ebbesen, S. D.; Zhang, W.; Mogensen, M. B. *ChemCatChem* **2014**, *6*, 1220−1224.